Journal of Geophysical Research: Planets

RESEARCH ARTICLE
10.1029/2018JE005744

Compositional Variations in the Vicinity of the Lunar Crust-Mantle Interface From Moon Mineralogy Mapper Data

M. Martinot[1,2], J. Flahaut[3], S. Besse[4], C. Quantin-Nataf[2], and W. van Westrenen[1]

[1]Faculty of Science, Vrije Universiteit Amsterdam, Amsterdam, The Netherlands, [2]Université de Lyon, UCBL, ENSL, CNRS, LGL-TPE, Villeurbanne, France, [3]Centre de Recherches Pétrographiques et Géochimiques, CNRS/Université de Lorraine, Vandoeuvre-lès-Nancy, France, [4]European Space Astronomy Centre, Villanueva de la Cañada, Madrid, Spain

Abstract Moon Mineralogy Mapper spectroscopic data were used to investigate the mineralogy of a selection of impact craters' central peaks or peak rings, in order to characterize the lunar crust-mantle interface, and assess its lateral and vertical heterogeneity. The depth of origin of the craters' central peaks or peak rings was calculated using empirical equations, and compared to Gravity Recovery and Interior Laboratory crustal thickness models to select craters tapping within +10/−20 km of the crust-mantle interface. Our results show that plagioclase is widely detected, including in craters allegedly sampling lower crustal to mantle material, except in central peaks where Low-Calcium Pyroxene was detected. Olivine detections are scarce, and identified in material assumed to be derived from both above and below the crust-mantle interface. Mineralogical detections in central peaks show that there is an evolution of the pyroxene composition with depth, that may correspond to the transition from the crust to the mantle. The correlation between High-Calcium Pyroxene and some pyroxene-dominated mixture spectra with the location of maria and cryptomaria hints at the existence of lateral heterogeneities as deep as the crust-mantle interface.

Plain Language Summary This study surveys the mineralogy of 36 lunar impact craters scattered across the lunar surface. All these craters present a central peak or peak ring, inherited from the impact, where material from depth was brought up to the surface. According to our calculations, these craters should sample material originating from as deep as the interface between the crust and the mantle (+10/−20 km). We make use of visible near-infrared spectroscopy (we investigate the light that is reflected from the lunar surface) in order to infer the central peaks compositions. We detected several minerals within the craters, including plagioclase, olivine, spinel, and pyroxene. An evolution of the composition of pyroxene (from High-Calcium to Low-Calcium) is observed with depth. We also demonstrate the presence of lateral heterogeneities within the crust and at the crust/mantle interface.

Key Points:
- Plagioclase is widely detected in the central peaks of craters allegedly sampling the lower crust or mantle, except where LCP is observed
- Lateral heterogeneities at the crust-mantle interface and a pyroxene compositional evolution with depth (from HCP to LCP) were observed
- This study's mineralogical observations support the GRAIL crustal thickness model 1 better than the model 3

Correspondence to:
M. Martinot,
m.martinot@vu.nl

Citation:
Martinot, M., Flahaut, J., Besse, S., Quantin-Nataf, C., & van Westrenenm, W. (2018). Compositional variations in the vicinity of the lunar crust-mantle interface from Moon mineralogy mapper data. *Journal of Geophysical Research: Planets*, *123*, 3220–3237. https://doi.org/10.1029/2018JE005744

Received 28 JUN 2018
Accepted 28 NOV 2018
Accepted article online 3 DEC 2018
Published online 27 DEC 2018

1. Introduction

Lunar crust composition and stratigraphy provide important constraints on our understanding of its origin and evolution (e.g., Jaumann et al., 2012). The Lunar Magma Ocean (LMO) hypothesis predicts that minerals crystallized in the order of olivine, Low-Calcium Pyroxene (LCP), then High-Calcium Pyroxene (HCP), and sank to the bottom of the magma ocean, forming the mantle and lower crust (e.g., Charlier et al., 2018; Elardo et al., 2011; Elkins-Tanton et al., 2011; Lin et al., 2017a, 2017b; Rapp & Draper, 2018; Snyder et al., 1992). During later stages of the magma ocean crystallization, lighter minerals like plagioclase formed an anorthositic (>90% anorthite-rich plagioclase) upper crust by floatation (e.g., Kaula, 1979; Warren, 1985). The last stage of the LMO predicts the crystallization of a deep crustal layer, widespread and uniformly distributed, enriched in incompatible elements, and called urKREEP (Potassium, Rare Earth Elements, Phosphorus) layer (Shearer et al., 2006).

A number of remote sensing studies have informed our knowledge of the lunar crust composition and stratigraphy (e.g., Donaldson Hanna et al., 2014; Lemelin et al., 2015; Ohtake et al., 2009; Song et al., 2013; Tompkins & Pieters, 1999), pointing at both vertical and lateral heterogeneities. Because they excavate material from depth, impact craters are a key to probing the composition of the deeper layers of the lunar crust, and its

vertical stratification. Several remote sensing studies have been carried out in order to characterize the lunar crust-mantle interface and possible occurrence of mantle material. Tompkins and Pieters (1999) used Clementine ultraviolet-visible camera multispectral data. Their results point at a compositionally diverse crust, with a very anorthositic upper crust, and an increase of mafic content with depth. They also found evidence for the presence of mafic plutons in the crust. On the contrary, Lemelin et al. (2015) used Kaguya Multiband Imager data, and found no clear evidence of increasing mafic content with depth within the crust. Pieters et al. (2011) used spectroscopic data from the Moon Mineralogy Mapper (M^3) instrument to study the Moscoviense impact basin and described so-called OOS rock types, defined by high abundances of Orthopyroxene, Olivine, and Mg-rich Spinel. They proposed several origins for the OOS lithologies: they might represent components of the deep crust or even the crust-mantle interface, or alternatively have an exogenic origin. The lack of mafic material observed in the 900 km Orientale basin peak rings led Head et al. (1993) and Pieters et al. (1993) to propose that the material composing the peak rings originates from the crust. This hypothesis was confirmed by a high spatial resolution spectroscopic study of Orientale basin revealing the overwhelming presence of pure anorthosite (>90 vol% plagioclase) in Orientale basin peak rings (Cheek et al., 2013).

Melosh et al. (2017) 3-D modeled the largest lunar impact basin (SPA, with a diameter exceeding 2,200 km Howard et al., 1974; Spudis et al., 1994), and showed that the SPA impact event sampled the upper mantle. Melosh et al. (2017) combined the results of the simulation with spectroscopic observations of the SPA ejecta blanket and concluded that the lunar upper mantle has a large LCP component. An alternative hypothesis is that the melt sheet produced by the SPA-forming event differentiated (e.g., Hurwitz & Kring, 2014; Morrison, 1998; Nakamura et al., 2009), masking any potential mantle signature.

Remote sensing studies have also identified lateral heterogeneities in the lunar crust. Jolliff et al. (2000) used global geochemical data derived from Clementine multispectral data and Lunar Prospector gamma ray data and showed that there are at least three terranes: the Procellarum KREEP Terrane (PKT), the Feldspathic Highlands Terrane (FHT), and the South-Pole Aitken Terrane. Ohtake et al. (2009) used spectroscopic data from the Kaguya Multiband Imager and identified a plagioclase-rich layer between 3 and 30 km deep in the lunar crust. Donaldson Hanna et al. (2014) used M^3 spectroscopic data and confirmed the wide detection of rocks of high plagioclase abundance where the crust is between 30 and 63 km thick.

Modeling work was performed by Head and Wilson (1992) in order to evaluate the proportion of magmatic intrusions in the lunar crust. They estimated that a maximum of 37% to 50% of the lower crust volume is intruded by plutons. The potential presence of magmatic intrusions in the crust should be taken into account when investigating the presence of lateral heterogeneities in the lunar crust through impact craters, because of the discontinuous sampling they provide.

Vertical and lateral variations of the lunar crust-mantle interface have been observed in previous studies, but it is still unclear if the crust-mantle transition is sharp or gradual, or if it occurs at the same depth locally, regionally, or globally. Four crustal thickness models were derived from the recent Gravity Recovery and Interior Laboratory (GRAIL) mission's data, assuming different crustal porosities, and adding a seismically determined constraint on the crustal thickness at the Apollo 12 and 14 landing sites (Wieczorek et al., 2013). The GRAIL crustal thickness models provide different absolute crustal values in each point, and predict an average crust thickness between 34 and 43 km (Wieczorek et al., 2013). The mineralogical results provided in the present survey could help to determine which GRAIL model estimates best the crustal thickness at the local, regional, or global scales. This study aims at further characterizing the vertical and lateral variations of the lunar crust-mantle interface, using the recent GRAIL crustal thickness models to select craters sampling that depth, and the M^3 spectroscopic data to assess the mineralogy of selected impact craters' central peaks or peak rings. This study focuses on a selection of craters tapping the crust-mantle interface, which is deeper than previously investigated (e.g., Lemelin et al., 2015; Tompkins & Pieters, 1999). The potential compositional changes of the crust-mantle interface are surveyed, with a selection of craters sampling material between +10 and −20 km around this interface according to the GRAIL crustal thickness models, and spread over a wide range of latitude and longitude.

2. Material and Methods

2.1. Data Sets

Spectroscopic data from the M^3 instrument were used to derive the mineralogy of selected craters' central peaks or peak rings. M^3 is a hyperspectral imager that acquired visible to near-infrared data of the lunar surface

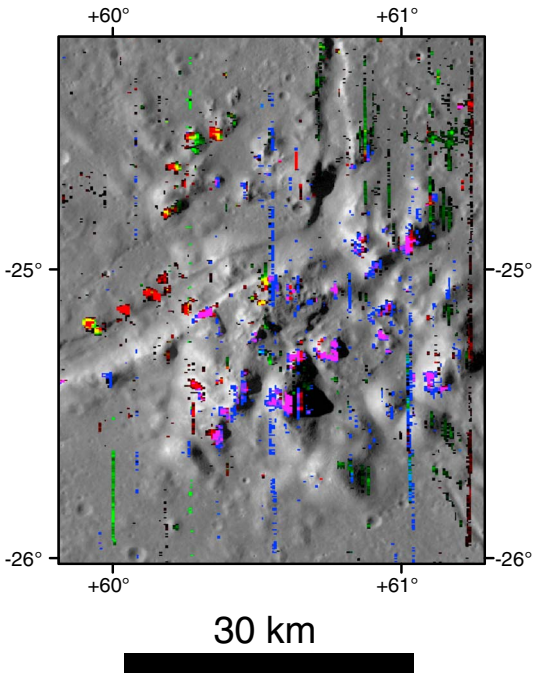

Figure 1. Color composite of Moon Mineralogy Mapper spectral parameters covering Petavius crater central peak, overlain on the Lunar Reconnaissance Orbiter Wide Angle Camera mosaic. The floor fractures described by Jozwiak et al. (2012) are merging in the central peak. R = area of the 1,000 nm absorption band; G = area of the 2,000 nm absorption band; B = position of the center of the 1,000 nm absorption band. The color composite was stretched in order to highlight the mineralogical diversity (R = 10.4–26.4; G = 30–52; B = 1230–1270 nm). The background image is the Lunar Reconnaissance Orbiter Wide Angle Camera mosaic. Olivine is displayed in red, pyroxene in green, and plagioclase in blue to pink shades, as its absorption band increases. Several vertical stripes of pixels are highlighted, which can be explained by the residual noise left after the Moon Mineralogy Mapper radiometric calibration.

between 2008 and 2009, with 85 spectral channels spanning from 430 to 3,000 nm (Pieters et al., 2009). The M^3 data used here are the calibrated data archived in the Planetary Data System (version 1 of Level 2), radiometrically corrected (Green et al., 2011), geometrically corrected (Boardman et al., 2011), thermally corrected (Clark et al., 2011), and photometrically corrected (Besse et al., 2013). Data from the optical period covering the maximal portion of each central peak were used, hence the wide variety of optical periods used (OP1B, OP2A, OP2C1, OP2C2, OP2C3, with a spatial resolution of 140 m per pixel for OP1B and OP2A; and 280 m per pixel for OP2C1, OP2C2, and OP2C3). This study is not comparing absolute reflectance of the surface from one crater to the other, so using data from several optical periods is not problematic.

Reflectance data at wavelengths lower than 620 nm were not considered because of the low signal-to-noise ratio recovered in this part of the spectrum (Green et al., 2011). Thermal effects start to appear at wavelengths beyond 2,700 nm, due to the contribution of the lunar surface (Clark et al., 2011). That is why reflectance data at wavelengths beyond 2,700 nm were not considered in this analysis. The continuum-removal algorithm developed by Martinot et al. (2018) was used. Their approach is similar to that of Horgan et al. (2014). The algorithm maximizes the area of lunar mafic minerals and plagioclase absorption bands at 1,000 and 2,000 nm. The continuum tie points are searched for in fixed intervals (620–1100, 1100–1660 nm) on a spectrum previously smoothed in order to limit noise influence on the tie point positions. A third tie point is fixed at 2,700 nm. Because of the presence of noise in the M^3 data, only band depths superior to 3% were considered in this study. Pixels with absorption band depths lower than 3% were masked out of the parameter maps. A complete list of output parameter maps is provided in Martinot et al. (2018). The predominantly used color composite for the mineralogical investigation was the one generated by Martinot et al. (2018) (R = area of the 1,000 nm absorption band; G = area of the 2,000 nm absorption band; B = position of the center of the 1,000 nm absorption band). Figure 1 shows a color composite of Petavius crater, classified as a floor fractured crater by Jozwiak et al. (2012). The color composite displays plagioclase in blue shades going toward pink, as its absorption band increases; olivine is highlighted in red; and pyroxene in bright green. The color composite was stretched using ENVI. The highlighted pixels were then manually checked and compared to reference spectra from the Reflectance Experiment LABoratory (RELAB) database in order to confirm any mineralogical detection. The color composites were then imported in a GIS software and compared with other existing data sets, specifically: the global mosaic of the Lunar Reconnaissance Orbiter Wide Angle Camera at 100 m per pixel, to visualize the geological context, and the Lunar Orbiter Laser Altimeter/SELENE Terrain Camera merged stereo-derived digital elevation model with a horizontal resolution of about 60 m per pixel, and a vertical accuracy of 4 m, providing information about the topography and elevation. Visible imagery was used to assess the central peak or peak ring morphology in order to confirm that the mineral detections occurred in uplifted material, and not in subsequently emplaced material such as later impact melts.

The GRAIL mission acquired gravimetric data from the Moon between 2011 and 2012. Four crustal thickness models were derived from the mission's data, with different assumptions on the crustal porosity and a constraint on the crustal thickness from the Apollo 12 and 14 landing sites' seismically determined crustal thickness (Wieczorek et al., 2013). GRAIL crustal thickness models 1 through 4 are reproduced in Figures 2a–2d. In this study, we will show the results of the models 1 and 3, which consider a crustal porosity of 12%, and respectively 29.9 and 38.1 km as crustal thickness constraint from the Apollo 12 and 14 landing sites. Absolute crustal thickness values from the models 1 and 2 and from the models 3 and 4 are close together (a few kilometers difference), which is why only models 1 and 3 were considered. The choice to compare mineralogical detections to models 1 and 3 over 2 and 4 is arbitrary.

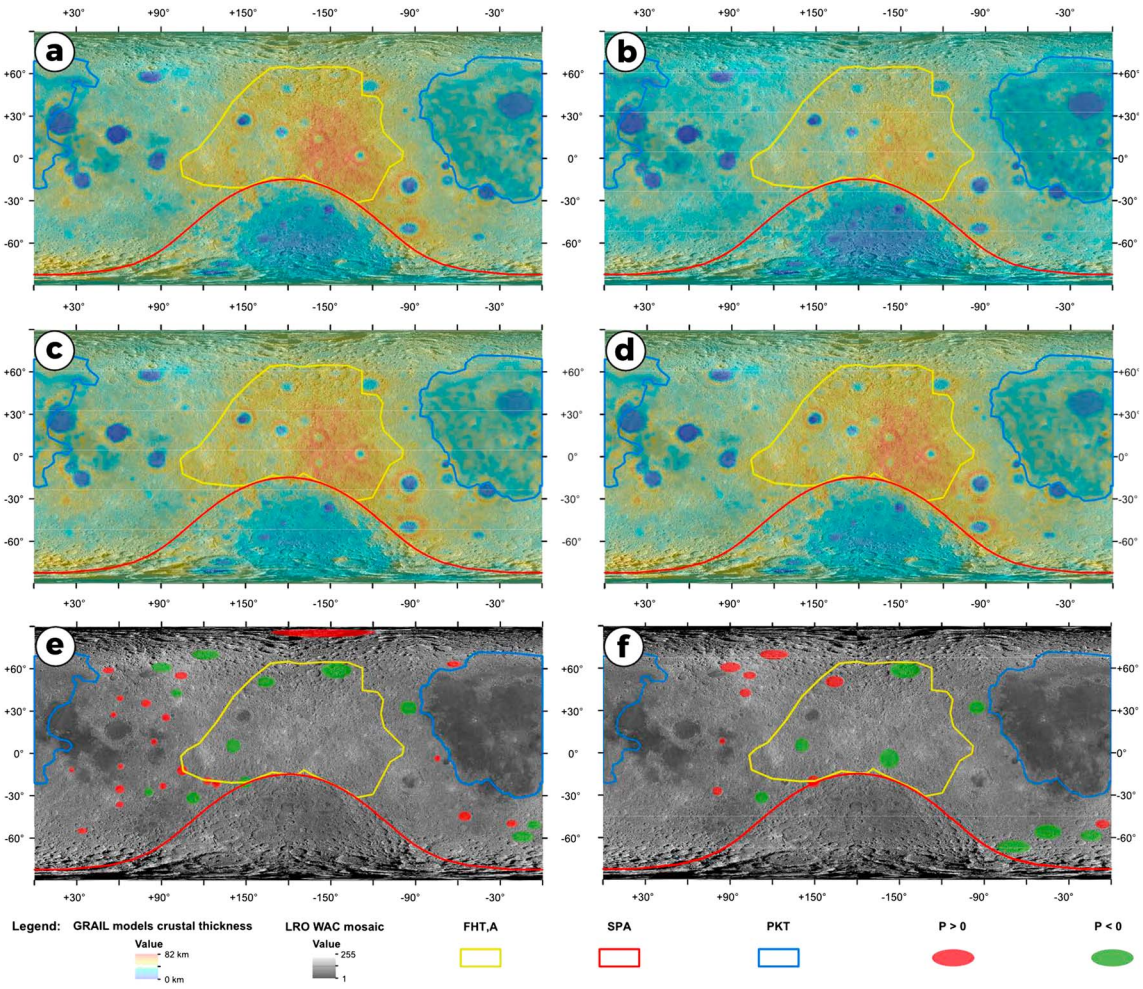

Figure 2. Global lunar crustal thickness maps from the GRAIL models 1 through 4, in panels (a) to (d) (Wieczorek et al., 2013). All crustal thickness maps are stretched between 0 and 82 km. The outlines of three major lunar terranes defined by Jolliff et al. (2000) are shown: the PKT in blue, the SPA basin in red, and the anorthositic FHT (FHT-a) in yellow. The outer FHT (FHT-o) was defined as the remainder of the lunar surface that is not part of the FHT-a, PKT, SPAT, or basin-filling mare (Jolliff et al., 2000). (e) Craters selected on the basis of the P_{cmi} value calculated with GRAIL crustal thickness model 1 and overlaid on the LRO WAC mosaic. Craters with a P_{cmi} value > 0 are symbolized as red circles, whereas craters with a P_{cmi} value < 0 are symbolized as green circles. (f) Craters selected on the basis of the P_{cmi} value calculated with GRAIL crustal thickness model 3 (see section 2.4) and overlaid on the LRO WAC mosaic. Craters with a P_{cmi} value > 0 are symbolized as red circles, whereas craters with a P_{cmi} value < 0 are symbolized as green circles. GRAIL = Gravity Recovery and Interior Laboratory; LRO WAC = Lunar Reconnaissance Orbiter Wide Angle Camera; PKT = Procellarum KREEP Terrane; SPAT = South-Pole Aitken Terrane.

A selection of complex craters and impact basins listed in the Lunar Impact Crater Database (LICD, Losiak et al., 2009, revised by Ohman at LPI) were examined in this study.

2.2. Lunar Minerals in the Crater Selection

The number of absorption bands and their position in spectroscopic data allow the identification of several minerals on the Moon. Plagioclase, olivine, pyroxene, and spinel were detected in the investigated craters.

Minor amounts of FeO (<1.0 wt%) can be incorporated into lunar calcic plagioclase (Burns, 1993), making it detectable with visible near-infrared spectroscopy. Iron-bearing plagioclase spectra are characterized by a single absorption band centered around 1,250 nm (Adams & Goullaud, 1978). However, in a mixture with mafic minerals such as olivine of pyroxene, plagioclase is easily masked: Cheek and Pieters (2014) showed that as little as 2 vol.% of olivine or pyroxene completely masks the plagioclase signal. Therefore, the detection of plagioclase in near-infrared spectra provides a constraint on the plagioclase content of the rock to be at least 85% (e.g., Cheek et al., 2013; Crown & Pieters, 1987).

Olivine spectra display a single, broad, and asymmetric absorption band centered at 1,050 nm (Sunshine & Pieters, 1998), shifting toward longer wavelength with increasing iron content (Burns, 1970). Sunshine and

Pieters (1998) showed that the absorption band of fayalite is broader and more flat-bottomed than that of forsterite and that this flattening of the absorption band can also be observed for large (<60 μm) forsterite grains. It is worth noting that some lunar olivine spectra can have an additional shallow absorption band near 2,000 nm caused by the presence of chromite (Isaacson et al., 2011).

Pyroxene spectra have two diagnostic absorption bands located around 1,000 and 2,000 nm (referred to as band 1 and band 2), shifting toward longer wavelengths with increasing iron or calcium content (Klima et al., 2007). LCP such as pigeonite or enstatite have an absorption band 1 centered at 900 nm and an absorption band 2 centered at 2,000 nm. HCP such as augite or diopside has absorption bands shifted toward longer wavelengths: its absorption band 1 is centered at 1,000 nm, and its absorption band 2 is centered at 2,200 or 2,300 nm (Adams, 1974).

Spinel spectra are characterized by a single broad absorption band, centered at 2,000 nm (Cloutis et al., 2004). Mg-spinel has a band 2 centered around 2,000 nm, and a third absorption band centered around 3,000 nm (Pieters et al., 2014).

2.3. Calculation of the Proximity Value to the Crust-Mantle Interface

GRAIL models were used together with Lunar Orbiter Laser Altimeter topography to calculate the proximity value to the mantle of all the complex craters listed in the LICD. The proximity to the crust-mantle interface (or material now exposed in a crater's central peak) was defined by Cahill et al. (2009) as the difference between the crustal thickness and the peak material depth of origin. In this study, it is referred to as the proximity value to the crust-mantle interface, or P_{cmi} value. The maximum depth of melting (D_m) was used to determine the minimum depth of origin of central peak material (Cintala & Grieve, 1998). The preimpact crustal thickness was calculated following the method in Flahaut et al. (2012), averaging the crustal thickness around the considered impact crater (from the Wieczorek et al., 2013, crustal thickness models) at a distance of one crater diameter, ±10% of the crater diameter.

If the P_{cmi} value is positive, only the crust should be chemically represented in the crater's central peak. If the P_{cmi} value is negative, material from below the crust-mantle interface was potentially sampled by the impact-forming event and emplaced in the resulting crater's central peak. Therefore, the P_{cmi} values symbolize the distance between the putative crust-mantle interface and the depth of origin of a crater's central peak material (see the Figure 1 from Flahaut et al., 2012).

2.4. Craters Selection

A subset of craters that presumably tap close to the crust-mantle interface was selected from the LICD, based on the following criteria: (1) the presence of an obvious central uplift structure (central peak or peak ring); (2) full or partial coverage of the central uplift structure by M^3 data; (3) a P_{cmi} value calculated with GRAIL crustal thickness models 1 or 3 between +10 and −20 km. A preliminary study showed that the mineralogical transition from crust to mantle does not seem sharp. Moreover, the complexity of the lunar surface may result in uncertainties in the precision of the craterisation equations, hence the wide P_{cmi} values interval investigated. Tracking the depth of origin of a central peak emplaced on a preexisting impact crater is not easily feasible. As a result, craters having their central peak located on the rim of a preexisting crater and craters located in the SPA basin were discarded from the selection. Based on these criteria, the mineralogy of 27 crater central peaks and 9 crater peak rings was studied. It is difficult to widen the pool of selected craters, because a large number of craters tapping the crust-mantle interface were eroded or subsequently filled by volcanic deposits. All the candidates that sample the crust-mantle interface, with M^3 coverage, were included in the present study. The selection of craters is listed in Table 1, together with the crater diameters; the crustal thickness of GRAIL models 1 through 4; the P_{cmi} values calculated from each GRAIL model; the melting depth (or central peak depth of origin, according to ; Cintala & Grieve, 1998); the excavation depth (or ejecta depth of origin, according to Cintala & Grieve, 1998); the M^3 optical period considered; and the crater age. The location of the selected craters are indicated in Figures 2e–2f.

3. Results

3.1. Mineralogical Detections

The mineralogical diversity of the 36 surveyed craters is summarized in Figure 4. Phases detected include plagioclase, olivine, HCP, LCP, spinel, pyroxene-dominated mixture spectra, and featureless spectra.

Journal of Geophysical Research: Planets

10.1029/2018JE005744

Table 1

Craters Selected for This Survey, Ranked According to P_{cmi} Values Calculated With the GRAIL Crustal Thickness Model 1, M1, From Greatest to Smallest Value; GRAIL Models 1 Through 4 Crustal Thickness; P_{cmi} Value Calculated With Each GRAIL Crustal Thickness Model; Peak Depth of Origin; Ejecta Depth of Origin; and Age of the Craters Studied During This Survey

			Diam.	GRAIL crust. thick. (km)				P_{cmi} value (km)				Melting depth	Excavation depth		
Name	LON	LAT	(km)	M1	M2	M3	M4	M1	M2	M3	M4	(km)	(km)	OP	Age
Fermi	122.6	−19.3	183	40.2	41.7	49.9	50.4	9.9	11.5	19.6	20.1	30.3	12.5	OP2C2	Pre-Nectarian
Riccioli	−74.6	−3.3	139	32.1	33.1	40.4	40.4	9.6	10.6	17.9	18.0	22.5	9.9	OP1B	Pre-Nectarian
Tsiolkovskiy	128.9	−21.2	185	39.9	41.3	49.5	49.8	9.3	10.7	18.9	19.2	30.6	12.6	OP2C1	Upper Imbrian
Messala	60.5	39.2	125	29.1	29.9	37.8	37.6	9.1	9.8	17.8	17.5	20.1	9.0	OP2C3	Pre-Nectarian
Pythagoras	−63.0	63.5	142	31.9	32.7	41.2	41.0	8.9	9.7	18.2	18.0	23.0	10.1	OP2A	Eratosthenian
Hommel	33.8	−54.7	126	29.0	29.7	37.1	36.8	8.8	9.5	16.9	16.6	20.2	9.1	OP2C1	Pre-Nectarian
Langrenus	61.1	−8.9	127	28.9	29.5	37.8	37.4	8.5	9.2	17.4	17.0	20.4	9.2	OP2C3	Eratosthenian
Furnerius	60.6	−36.0	135	30.0	30.8	38.4	38.2	8.2	9.0	16.6	16.4	21.8	9.7	OP2C3	Pre-Nectarian
de la Rue	52.3	59.1	134	29.8	30.5	38.6	38.3	8.2	8.8	17.0	16.6	21.6	9.6	OP1B	Pre-Nectarian
Theophilus	26.4	−11.4	110	23.8	24.5	31.4	31.2	6.3	7.0	13.9	13.7	17.5	8.1	OP1B	Eratosthenian
Longomontanus	−21.8	−49.6	157	31.9	32.7	40.4	40.2	6.2	7.0	14.7	14.6	25.6	11.0	OP1B	Nectarian
Cleomedes	56.0	27.7	125	25.9	26.5	34.1	33.7	5.9	6.5	14.0	13.7	20.1	9.0	OP1B	Nectarian
Curie	91.0	−22.9	151	30.1	30.8	38.6	38.4	5.5	6.3	14.0	13.8	24.6	10.6	OP2C1	Pre-Nectarian
Joliot	93.1	25.8	164	32.2	33.0	41.6	41.4	5.3	6.2	14.7	14.6	26.9	11.4	OP2C1	Pre-Nectarian
Rozhdestvenskiy	−155.4	85.2	177	33.4	34.2	42.2	42.0	4.2	5.0	13.0	12.8	29.2	12.1	OP2A	Pre-Nectarian
Neper	84.6	8.5	137	24.2	24.6	32.2	31.7	2.0	2.5	10.0	9.6	22.1	9.8	OP2C1	Nectarian
Schickard	−55.3	−44.3	206	36.2	37.3	45.9	45.9	1.8	2.9	11.5	11.5	34.4	13.8	OP2A	Pre-Nectarian
Pasteur	104.6	−11.9	224	39.4	40.9	49.6	49.9	1.8	3.2	11.9	12.3	37.6	14.8	OP2C1	Pre-Nectarian
Gauss	79.0	35.7	177	30.8	31.7	39.6	39.5	1.6	2.5	10.4	10.3	29.2	12.1	OP2C1	Nectarian
Petavius	60.4	−25.1	188	32.8	33.7	42.1	42.0	1.6	2.6	11.0	10.9	31.2	12.8	OP2C3	Lower Imbrian
Compton*	103.8	55.3	162	26.9	27.4	34.6	34.2	0.4	0.8	8.1	7.6	26.5	11.3	OP2C1	Lower Imbrian
Fabry	100.7	42.9	184	30.43	31.3	38.8	38.8	0.0	0.9	8.3	8.3	30.4	12.6	OP2C1	Pre-Nectarian
Humboldt*	80.9	−27.0	189	30.1	30.9	38.8	38.7	−1.2	−0.4	7.5	7.3	31.3	12.8	OP2C1	Upper Imbrian
Maginus	−6.3	−50.5	194	30.2	30.9	38.6	38.2	−2.0	−1.4	6.4	6.0	32.2	13.1	OP1B	Pre-Nectarian
Bel'kovich	90.2	61.1	214	30.7	31.3	39.5	39.0	−5.1	−4.6	3.7	3.2	35.8	14.3	OP2C1	Nectarian
Gagarin	149.2	−20.2	265	36.9	38.2	45.8	46.1	−8.2	−7.0	0.7	1.0	45.1	17.1	OP2C1	Pre-Nectarian
Clavius	−14.1	−58.8	245	32.3	33.1	40.8	40.7	−9.2	−8.4	−0.6	−0.8	41.5	16.0	OP1B	Nectarian
d'Alembert	163.9	50.8	248	40.5	41.8	49.9	50.0	−1.5	−0.3	7.8	8.0	42.0	16.2	OP2C1	Nectarian
Schwarzschild	121.2	70.1	212	30.2	30.8	38.3	38.0	−5.3	−4.6	2.8	2.5	35.5	14.2	OP2C1	Nectarian

Journal of Geophysical Research: Planets

10.1029/2018JE005744

Table 1 *Continued*

Name	LON	LAT	Diam. (km)	GRAIL crust. thick. (km) M1	M2	M3	M4	P_{cmi} value (km) M1	M2	M3	M4	Melting depth (km)	Excavation depth (km)	OP	Age
Milne	112.2	−31.4	272	34.3	35.2	43.4	43.2	−12.2	−11.2	−3.1	−3.2	46.4	17.5	OP2C2	Pre-Nectarian
Mendeleev	140.9	5.7	313	41.8	43.3	51.4	51.9	−12.3	−10.8	−2.6	−2.2	54.0	19.7	OP2C1	Nectarian
Bailly	−69.1	−66.5	287	35.0	35.9	44.0	43.9	−14.2	−13.3	−5.2	−5.3	49.20	18.3	OP2C1	Nectarian
Lorentz	−95.3	32.6	312	34.5	35.5	43.3	43.3	−19.4	−18.4	−10.6	−10.5	53.8	19.6	OP1B	Pre-Nectarian
Birkhoff	−146.1	58.7	345	39.6	40.7	48.8	48.8	−20.4	−19.3	−11.2	−11.2	60.0	21.4	OP2C2	Pre-Nectarian
Schiller-Zucchius	−45.0	−56.0	335	35.8	36.8	45.0	45.0	−22.3	−21.4	−13.2	−13.2	58.1	20.9	OP1B	Pre-Nectarian
Korolev	−157.4	−4.0	437	48.7	50.5	59.1	59.8	−28.8	−27.0	−18.4	−17.7	77.5	26.1	OP2C1	Nectarian

Note. Craters with * were listed by Baker et al. (2011) as transition crater (Compton crater) and crater with ring-like central peak (Humboldt crater). Crater locations, diameter, melting depth, excavation depth, and age are from the Lunar Impact Crater Database; GRAIL crustal thickness models from Wieczorek et al. (2013). Note that the table separates the central peak craters, at the top of the table, from the peak ring craters, at the bottom of the table. GRAIL = Gravity Recovery and Interior Laboratory.

Plagioclase was detected in 17 out of 36 craters (Figures 3a–3b), and selected plagioclase spectra are shown in Figure 4a. Olivine was detected in 3 out of 36 craters (Figures 3c–3d). The narrow absorption band and its right shoulder on the spectra in Figure 4b are compatible with a forsteritic composition. The asymmetry and ratio between the band 1 depth and the band 2 depth of Humboldt and Petavius spectra is compatible with olivine. The shallow absorption band observed near 2,000 nm may be caused by the presence of chromite (Isaacson et al., 2011), or small amounts of pyroxene (Mustard & Pieters, 1987).

LCP was detected in 3 out of 36 craters (Figures 3e–3f), and the spectra are displayed in Figure 3c. HCP was observed in 4 out of 36 craters (Figures 3e–3f), and the spectra are shown in Figure 4d. Spectra displaying two absorption bands which band 1 and 2 centers are close to but different from the LCP or HCP spectra field of values from Horgan et al. (2014) and Martinot et al. (2018) were labeled as pyroxene-dominated mixture spectra. Pyroxene-dominated mixture spectra were observed in 20 out of 36 craters (Figures 3g–3h). A selection of spectra is shown in Figure 4e, with the LCP and HCP fields represented in light gray and dark gray, respectively. A continuum-removal error could cause a displacement of the band centers, but in the case of the pyroxene-dominated mixture spectra, the bands are broad and strong, which strongly suggests a pyroxene-dominated mixture composition.

Spinel spectra were observed in 3 out of 36 craters (Figure 3c). Spectra are shown in Figure 4f. Spinel was not found in the central peaks of the craters selected with the GRAIL crustal thickness model 3.

Spectra with no diagnostic 1,000 and 2,000 nm absorption bands were reported in previous studies as featureless spectra (e.g., Hawke et al., 2003; Spudis et al., 1984; Yamamoto et al., 2015). The study of reflectance spectra from shocked plagioclase showed that the weakening and disappearance of plagioclase absorption band can be caused by shock pressures (Adams et al., 1979; Bruckenthal & Pieters, 1984), or space weathering of plagioclase (Lucey, 2002). Locations of featureless spectra detections, observed in 14 out of 36 craters, are shown in Figures 3a–3b. Featureless spectra, which could correspond to shocked or weathered plagioclase, are presented in Figure 4g.

Spectra observed in Curie and Gagarin craters have shallow absorption features that do not correspond to any typical lunar mineral (plagioclase, HCP, LCP, olivine, or spinel) and are different from featureless spectra. Such spectra were labeled as spectra with no particular signature. Examples of spectra detected in Curie and Gagarin are shown in Figure 4h.

3.2. Lateral Distribution

The locations of all mineralogical occurrences are summarized in Figure 3. Multiple mineralogical detections are observed in the central peak or peak ring of several craters. Plagioclase, featureless spectra, and pyroxene-dominated mixture spectra occurrences are widely detected in the selected craters. A few plagioclase and featureless spectra are located near the edge of the PKT (in Pythagoras, Lorentz, Riccioli, and Theophilus craters), but most detections are located in the FHT-o. Olivine, spinel, and HCP detections are concentrated in a relatively restricted latitude and longitude range: 30°N, 35°S; 20°W, 100°E, located in the FHT-o LCP was scarcely detected in the selected craters. Two detections are located in Clavius and Maginus craters, near the edge of the South-Pole Aitken Terrane, and one occurrence is found in d'Alembert crater, in the FHT-a.

3.3. Vertical Distribution

Table 2 shows the mineralogical detections of the selection of impact craters sorted by decreasing P_{cmi} value obtained with the GRAIL crustal thickness model 1 (i.e., decreasing distance to the crust-mantle interface). Featureless spectra are detected at all studied P_{cmi} values. Plagioclase is widely detected, even in impact craters supposedly sampling mantle material, except in crater central peaks where LCP is observed. The plagioclase detection associated to the lowest P_{cmi} value in a central peak crater is located in Humboldt crater. The three olivine occurrences are concentrated in a P_{cmi} value interval ranging from +6.3 to −1.2 km, as calculated with GRAIL crustal thickness model 1, and +13.9 and +7.5 km as calculated with GRAIL crustal thickness model 3. The three spinel detections are clustered in a narrower P_{cmi} value range, ranking from +6.3 to +2.0 km with GRAIL crustal thickness model 1, and +13.9 and 10.0 km with GRAIL crustal thickness model 3. The HCP detections occur between +8.5 and 0.0 km with GRAIL crustal thickness model 1, and +17.4 and +8.3 km with GRAIL crustal thickness model 3. The LCP detections range from −1.5 to −9.2 km with GRAIL crustal thickness model 1, and +7.8 to −0.6 km with GRAIL crustal thickness model 3. Pyroxene-dominated mixture detections occur at all investigated P_{cmi} values, except where LCP is detected.

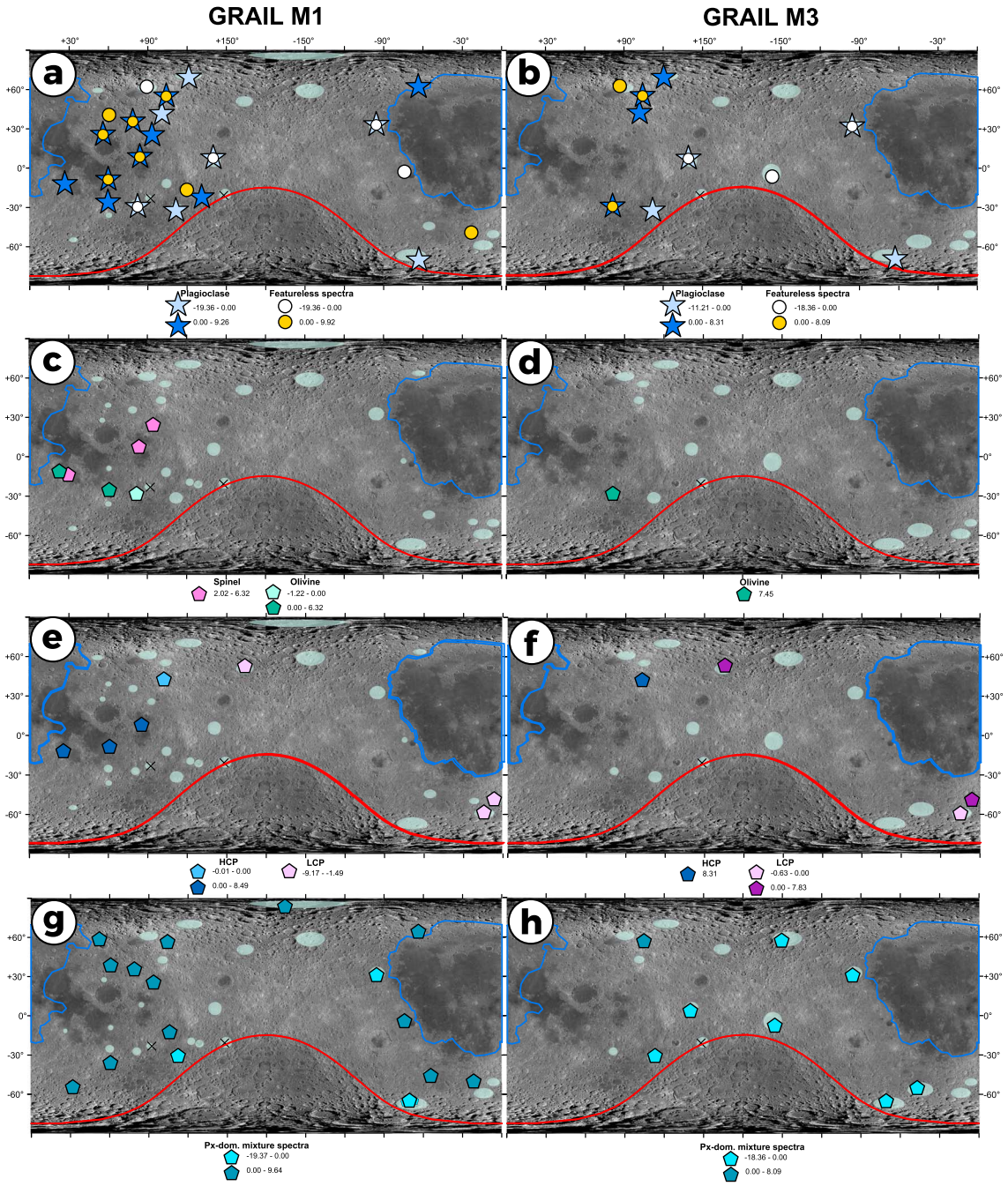

Figure 3. Mineralogical detections on the selected craters' central peak or peak ring, overlaid on Lunar Reconnaissance Orbiter Wide Angle Camera global mosaic. The red line materializes the border of the South-Pole Aitken Terrane defined by Jolliff et al. (2000). Detections in craters having P_{cmi} values < 0 are represented with light colored symbols, whereas detections in craters having P_{cmi} values > 0 are represented with dark colored symbols. The circles represent the craters selected with the GRAIL crustal thickness models 1 and 3, overlaid on the Lunar Reconnaissance Orbiter Wide Angle Camera global mosaic. The black crosses symbolize the craters where no clear mineralogical detection was observed. (a). Plagioclase and/or featureless spectra occurrences in the craters selected with GRAIL model 1. (b). Plagioclase and/or featureless spectra occurrences in the craters selected with GRAIL model 3. (c). Olivine and spinel occurrences in the craters selected with GRAIL model 1. (d). Olivine occurrences in the craters selected with GRAIL model 3. (e). HCP and LCP occurrences in the craters selected with GRAIL model 1. (f). HCP and LCP occurrences in the craters selected with GRAIL model 3. (g). Pyroxene-dominated mixture detections in the craters selected with GRAIL model 1. (h). Pyroxene-dominated mixture detections in the craters selected with GRAIL model 3. GRAIL = Gravity Recovery and Interior Laboratory; HCP = High-Calcium Pyroxene; LCP = Low-Calcium Pyroxene.

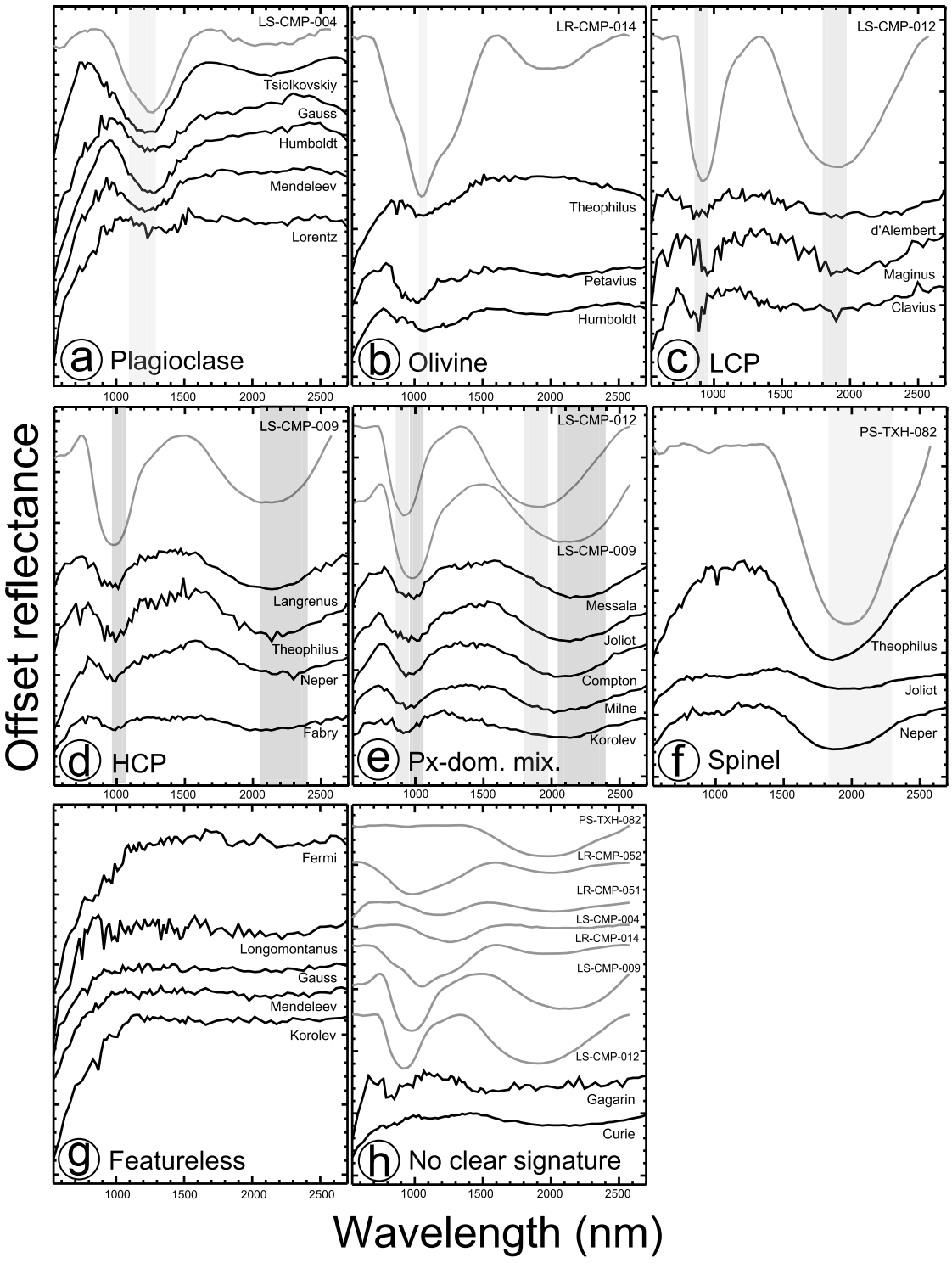

Figure 4. Representative continuum removed spectra showing the mineralogical diversity encountered in the selected craters. Black spectra are from the Moon Mineralogy Mapper observations; gray spectra are the corresponding RELAB database spectra. The gray areas materialize the diagnostic absorption regions for each mineral. (a) Plagioclase spectra. (b) Olivine spectra. (c) LCP spectra. (d) HCP spectra. (e) Pyroxene-dominated mixture spectra. (f) Spinel spectra. (g) Featureless spectra. (h) Spectra with no particular mineralogical signature (observed in Curie and Gagarin craters). Laboratory spectra from the RELAB database were added in order to show that the observed spectra do not correspond to known lunar mineralogical detections (spectra, from top to bottom: spinel, green glass, orange glass, plagioclase, olivine, HCP, LCP). LCP = Low-Calcium Pyroxene; HCP = High-Calcium Pyroxene.

Journal of Geophysical Research: Planets

10.1029/2018JE005744

Table 2

P_{cmi} Value Calculated With Each Gravity Recovery and Interior Laboratory Crustal Thickness Model of the Craters Studied in This Survey, Sorted Against the P_{cmi} Value Calculated With Gravity Recovery and Interior Laboratory Crustal Thickness Model 1 (From Greatest to Smallest Value)

	P_{cmi} value (km)				Mineralogical detections						
Name	M1	M2	M3	M4	Plagioclase	Featureless	Pyroxene-dominated mixture	HCP	LCP	Olivine	Spinel
Fermi	9.9	11.5	19.6	20.1		X					
Riccioli	9.6	10.6	17.9	18.0		X	X				
Tsiolkovskiy	9.3	10.7	18.9	19.2	X						
Messala	9.1	9.8	17.8	17.5		X	X				
Pythagoras	8.9	9.7	18.2	18.0	X		X				
Hommel	8.8	9.5	16.9	16.6			X				
Langrenus	8.5	9.2	17.4	17.0	X	X		X			
Furnerius	8.2	9.0	16.6	16.4			X				
de la Rue	8.2	8.8	17.0	16.6			X				
Theophilus	6.3	7.0	13.9	13.7	X			X		X	X
Longomontanus	6.2	7.0	14.7	14.6		X	X				
Cleomedes	5.9	6.5	14.0	13.7	X	X					
Curie	5.5	6.3	14.0	13.8							
Joliot	5.3	6.2	14.7	14.6	X		X				X
Rozhdestvenskiy	4.2	5.0	13.0	12.8			X				
Neper	2.0	2.5	10.0	9.6	X	X		X			X
Schickard	1.8	2.9	11.5	11.5			X				
Pasteur	1.8	3.2	11.9	12.3			X				
Gauss	1.6	2.5	10.4	10.3	X	X	X				
Petavius	1.6	2.6	11.0	10.9	X					X	
Compton*	0.4	0.8	8.1	7.6	X	X	X				
Fabry	0.0	0.9	8.3	8.3	X			X			
Humboldt*	−1.2	−0.4	7.5	7.3	X	X				X	
Maginus	−2.0	−1.4	6.4	6.0					X		
Bel'kovich	−5.1	−4.6	3.7	3.2		X					
Gagarin	−8.2	−7.0	0.7	1.0							
Clavius	−9.2	−8.4	−0.6	−0.8					X		
d'Alembert	−1.5	−0.3	7.8	8.0					X		
Schwarzschild	−5.3	−4.6	2.8	2.5	X						
Milne	−12.2	−11.2	−3.1	−3.2	X		X				
Mendeleev	−12.3	−10.8	−2.6	−2.2	X	X	X				
Bailly	−14.2	−13.3	−5.2	−5.3	X		X				
Lorentz	−19.4	−18.4	−10.6	−10.5	X	X	X				
Birkhoff	−20.4	−19.3	−11.2	−11.2	X		X				
Schiller-Zucchius	−22.3	−21.4	−13.2	−13.2			X				
Korolev	−28.8	−27.0	−18.4	−17.7	x	X	X				

Note. The first part of the table shows craters with central peak, and the second part of the table lists all craters described as peak ring craters by Baker et al. (2011). The presence of a mineralogical detection on the central peak and/or peak ring (plagioclase, featureless spectra, HCP, pyxoxene-dominated mixture spectra, LCP, olivine, or spinel) is symbolized by a cross. Previous plagioclase occurrences detected by ?DonaldsonHanna2014,Yamamoto2010 (, DonaldsonHanna2014,Yamamoto2010) or Yamamoto et al. (2012), as well as this study is denoted as X. Previous plagioclase occurrences detected by Yamamoto et al. (2010), but not our study, are denoted as x. Craters with * were listed by Baker et al. (2011) as transition crater (Compton crater) and crater with ring-like central peak (Humboldt crater). Note that the table separates the central peak craters, at the top of the table, from the peak ring craters, at the bottom of the table. LCP = Low-Calcium Pyroxene; HCP = High-Calcium Pyroxene.

Table 3
Table Comparing the P_{cmi} Values Range Considered in Previous Studies (That Used a Different Set of Craters) and This Survey

Tompkins and Pieters (1999)	GRAIL M1	GRAIL M3
P_{cmi}max (km)	+46.2	+57.4
P_{cmi}min (km)	+0.4	+8.1
Lemelin et al. (2015)	GRAIL M1	
P_{cmi}max (km)	+41.1	
P_{cmi}min (km)	+1.6 (and von Kármán, in SPA, with $P_{cmi} = -11.4$)	
Our study	GRAIL M1	GRAIL M3
P_{cmi}max (km)	+10.0	+10.0
P_{cmi}min (km)	−20.0	−20.0

Note. The P_{cmi} values were calculated using the GRAIL crustal thickness models, and the maximum depth of melting as the minimum depth of origin of the central peak material. GRAIL = Gravity Recovery and Interior Laboratory.

4. Discussion

4.1. Methods Limitations

The lunar crust-mantle interface and its lateral and vertical compositional structure are investigated in this study. However, some limits have to be kept in mind when considering the results presented here: (1) while the relative GRAIL crustal thickness variations are robust, there can be a difference of >10 km in the absolute crustal thickness values from one model to the other; (2) the melting depth and other the craterisation equations were empirically determined, which can introduce a nonnegligible error in the calculation of the proximity value to the crust-mantle interface; (3) the central peak likely contains mixed material that originate from shallower depths than the maximum depth of melting. This implies that shallow layers of the crust can be represented in the central peak.

4.2. Previous Studies' Craters P_{cmi} Calculation and Comparison to the Present Survey Crater Selection

Previous surveys (Lemelin et al., 2015; Tompkins & Pieters, 1999) have examined craters sampling deep crustal to mantle material. Here we focus on a specific depth range that presumably includes the transition from the lower crust to the mantle and the potential urKREEP layer.

In order to enable comparison with previous works, the P_{cmi} values of the craters surveyed in Tompkins and Pieters (1999) and Lemelin et al. (2015) were calculated using the method presented here (the maximum depth of melting representing the minimum depth of origin of the central peak material, and the GRAIL models providing the crustal thickness). Table 3 presents the P_{cmi} value range considered in their studies and the present survey. Tompkins and Pieters (1999) investigated craters presumably tapping crustal material, while Lemelin et al. (2015) surveyed craters sampling deeper material. It is worth noting that the crater sampling deepest material in Lemelin et al. (2015) selection, von Kármán crater, is located in the SPA basin, where a thick impact melt sheet was formed during the impact event (Morrison, 1998). The next crater in their selection (Petavius crater) has a P_{cmi} value of +1.6 km. The craters surveyed in the present study are therefore supposedly tapping deeper material than the craters investigated in previous studies.

4.3. Spinel and Olivine Detections

Table 2 and Figure 5 show that spinel and olivine are concentrated in a latitude and longitude range in the FHT-o defined by Jolliff et al. (2000), and a P_{cmi} value range between +6.3 and −1.2 km as calculated with GRAIL crustal thickness model 1, and +13.9 and +7.5 km as calculated with GRAIL crustal thickness model 3. According to Pieters et al. (2011), olivine and spinel could have a lower crustal origin. Gross et al. (2011) proposed that spinel could have formed in the lunar crust by magma-wall rock interactions, and Vaughan et al. (2013) suggested that the crystallization of a melt mixture between the anorthositic crust and mantle could form spinel. Spinel could alternatively have formed in the final stages of the LMO solidification: Lin et al. (2017b) performed water-bearing LMO crystallization experiments and showed that spinel is among the last minerals to be crystallized during solidification of a water-bearing magma ocean. According to their calculation, a spinel-bearing layer could be found around 30 km underneath the surface after magma ocean solidification. The urKREEP layer being the last layer to crystallize from LMO solidification (Shearer et al., 2006), it could be stratigraphically linked or mingled with such a spinel-bearing layer. Warren and Wasson (1979)

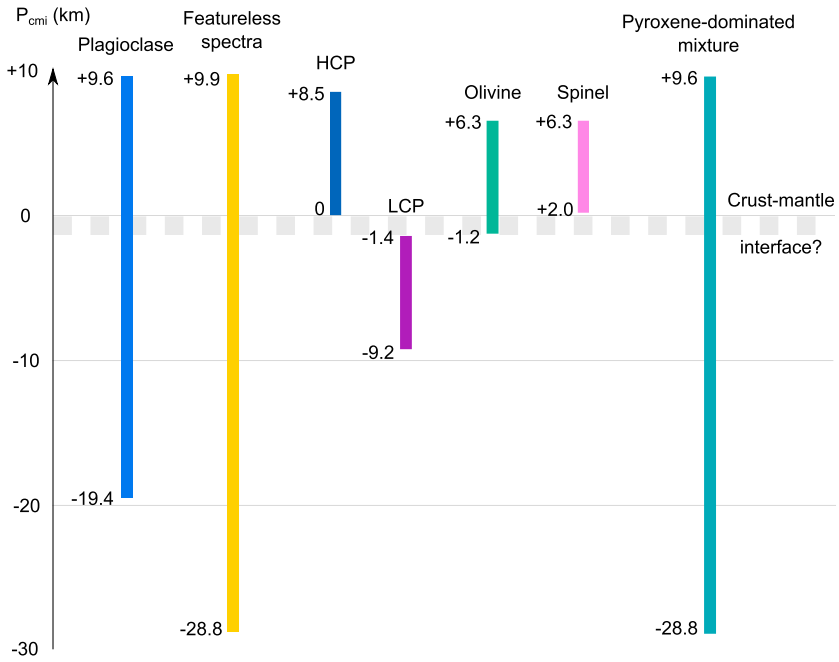

Figure 5. Schematic view of the crust-mantle interface presenting the mineralogical detections as a function of the P_{cmi} as calculated with Gravity Recovery and Interior Laboratory crustal thickness model 1. The gray dotted line symbolizes the possible crust-mantle interface. HCP = High-Calcium Pyroxene; LCP = Low-Calcium Pyroxene.

estimated that a global urKREEP layer would be thinner than 2 km, whereas Wieczorek and Phillips (2000) proposed that it was unevenly distributed and concentrated under the PKT region instead.

If the surveyed craters where spinel is observed sample depths around 30 km, they may tap this final LMO solidification layer. In the craters where spinel is observed, the minimal depth of origin of the central peak material (maximum depth of melting, Cintala & Grieve, 1998) ranges from 17.5 to 26.9 km (Theophilus: 17.5 km; Neper: 22.1 km; Joliot: 26.9 km). However, 11 other craters sampling a depth between 25 and 35 km are included in the study (Compton, Fabry, Fermi, Gauss, Humboldt, Longomontanus, Maginus, Petavius, Rozhdestvenskiy, Schickard, Tsiolkovskiy), and spinel was not detected in any of those, suggesting it might not be a continuous layer. Instead, these central peaks show the presence of plagioclase, pyroxene-dominated mixture spectra, or LCP.

Olivine is observed in craters supposedly sampling material from above and below the crust-mantle interface, according to GRAIL crustal thickness model 1. However, olivine detections are scarce in the craters studied here (only 3 craters out of 36) and does not appear to have a major role in the transition from the crust to the mantle. This is consistent with the recent study by Melosh et al. (2017), who proposed that the lunar upper mantle has a large LCP component instead of olivine signatures.

Albeit surveying craters supposedly tapping around the crust-mantle interface, where the urKREEP layer would allegedly be observed, we found no evidence of a mineralogically distinct, global urKREEP layer. Our observations rather support the presence of lateral heterogeneity in the crust. Olivine and spinel could have a plutonic origin (Head & Wilson, 1992). Pieters et al. (2014) described the spinel occurrences in Joliot and Theophilus crater as Pink Spinel Anorthosite (feldspar-dominated rock with Mg-spinel and less than 5% mafic minerals) and proposed that Pink Spinel Anorthosite originates from the lower crust, which is in agreement with the Lin et al. (2017b) experiments.

4.4. Plagioclase Detections

Figure 5 shows that pure plagioclase occurrences are widely detected, even in craters supposedly tapping lower crustal to mantle material (e.g., in Humboldt crater central peak), except in the central peaks where LCP is observed. This means that plagioclase-rich rocks are present in the lower crust. One could interpret the lack of plagioclase occurrence (crustal material) in the central peaks where LCP is observed as evidence that mantle material is emplaced in the central peaks, and place the crust-mantle interface at P_{cmi} values between those

of Humboldt and Maginus craters. However, plagioclase being spectrally nearly transparent, its presence may be masked by LCP. An alternative explanation to the presence of LCP could be that the craters where it is observed are tapping plutons.

In craters where plagioclase was observed, the minimal depth of origin of the central peak material ranges from 17 to 60 km, which is consistent with the existence of a widespread purest anorthositic layer (>98 vol% plagioclase) that was proposed by Ohtake et al. (2009), Yamamoto et al. (2012), and Donaldson Hanna et al. (2014). However, HCP, pyroxene-dominated mixture spectra, spinel, or olivine were also detected in most of the surveyed central peaks where purest anorthosite was detected in previous studies (Donaldson Hanna et al., 2014; Yamamoto et al., 2010, 2012). A pure anorthositic layer may exist and be mixed with mafic material originating from other crustal depths in the surveyed central peaks during the impact event. Alternatively, the anorthositic crust may be intruded later by more mafic plutons. Head and Wilson (1992) proposed that as much as 50% of the lower crust is intruded by plutons; and Dygert et al. (2017) proposed that the present-day lunar crust is composed of a relatively impure, old crust, later intruded by pure anorthositic diapirs. Both processes are consistent with the observation of PAN occurrences juxtaposed to mafic detections.

4.5. Pyroxene Detections

All pyroxene detections with regards to the crust-mantle interface are shown in Figure 5. Pyroxene-dominated mixture spectra are widely detected in the crust, except in the central peaks or peak rings where HCP or LCP can be identified. The pyroxene-dominated mixture spectra observed in this study have a band 1 center close to the LCP band 1 center values, and a band 2 center that is in the region of the HCP band 2 center. This could result from a mixture of pyroxene and other minerals, resulting in the shift of the absorption band centers beyond the LCP or HCP fields.

The P_{cmi} values associated to this study's HCP and LCP detections show a clear vertical progression: the HCP detections are concentrated in a range of P_{cmi} values that is shallower than that of the LCP detections (+8.5 to 0 km with GRAIL crustal thickness model 1, and +17.4 to +8.3 km with GRAIL crustal thickness model 3 for the HCP detections; and −1.5 to −9.2 km with GRAIL crustal thickness model 1, and +7.4 and −0.6 km with GRAIL crustal thickness model 3 for the LCP detections).

This supports Tompkins and Pieters (1999) observations of an LCP-enrichment with depth. It is worth noting that no other mineral is detected in central peaks where LCP is observed, and the transition from HCP to LCP happens very close to the model crust-mantle interface. This points to the potential existence of a deep LCP-rich crustal (or upper mantle) layer, consistent with Melosh et al. (2017) simulations.

The P_{cmi} values of the first crater where LCP is observed are −2.0 km with GRAIL crustal thickness model 1, and +6.4 km with GRAIL crustal thickness model 3. LCP is observed in the central peaks of two of the central peak craters supposedly tapping the deepest material in the crater selection (Maginus and Clavius craters). Craters with more negative P_{cmi} values were studied, but these craters have peak rings instead of central peaks. According to Baker and Head (2015) and Miljković et al. (2017), the maximum depth of melting for peak ring basins cannot be taken as a proxy for estimating the depth of origin of the material exposed in the peak rings. Therefore, the P_{cmi} values calculated for the peak ring craters of this study may not be appropriate reflections of the exhumation process. This is strengthened by the results of a spectroscopic survey of Orientale basin peak rings by Cheek et al. (2013), finding that Orientale basin peak rings are composed of pure anorthositic material. Cheek et al. (2013) confirmed the hypothesis that the material composing the Orientale basin peak rings originated from the crust (Head et al., 1993; Pieters et al., 1993). All peak ring craters apart from d'Alembert and Schiller-Zucchius display plagioclase in their peak ring, which confirms their crustal origin. The mafic detections in d'Alembert and Schiller-Zucchius peak rings may be caused by the sampling of plutons at depth.

4.6. Comparison Between Pyroxene Detections and Mare/Cryptomare Locations

Figure 6 shows the location of maria and cryptomaria on the Moon, with this study's pyroxene detections (shapefiles from Whitten & Head, 2015). Cryptomare were defined by Head and Wilson (1992) as mare deposits that were subsequently covered by higher albedo deposits. All pyroxene detections in craters located near maria or cryptomaria have a HCP or pyroxene-dominated mixture spectra signature. In some craters, the HCP or pyroxene-dominated mixture spectra occurrences are located near the bottom of the central peak. The altitude difference between the HCP or pyroxene-dominated mixture spectra detections and the crater floor can be as low as 2 km. In these instances, contamination by surficial volcanic units is possible. The P_{cmi} value

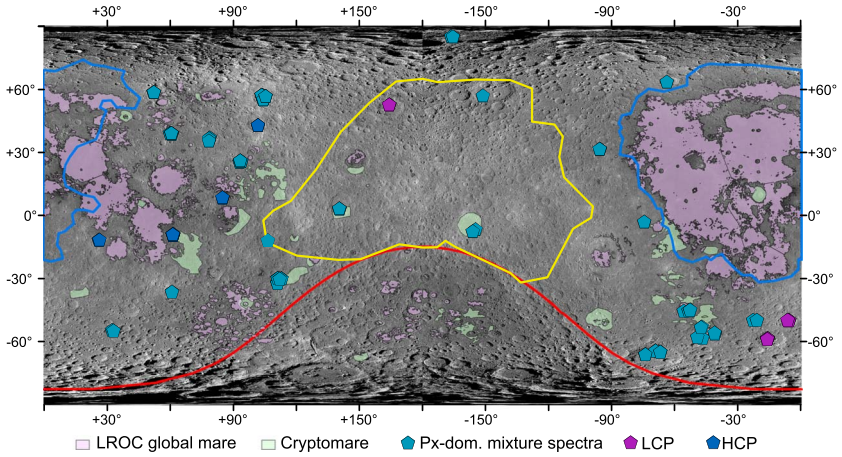

Figure 6. Global map with maria and cryptomaria locations (from the LRO archive and Kring et al. (2012), *Appendix Table 2.3*, for a summary of cryptomaria locations from the literature) and all pyroxene detections of this study. The background image is the Lunar Reconnaissance Orbiter Wide Angle Camera global mosaic. The outlines of three major lunar terranes defined by (Jolliff et al., 2000) are shown: the Procellarum KREEP Terrane in blue, the South-Pole Aitken basin in red, and the anorthositic Feldspathic Highlands Terrane in yellow. LCP = Low-Calcium Pyroxene; HCP = High-Calcium Pyroxene.

range considered in this study highlights the crust-mantle interface. If the central peak and peak rings were not contaminated by surficial volcanic units, the link between maria and cryptomaria locations (which have a pyroxene signature) and HCP and some pyroxene-dominated mixture detections may point at the presence of lateral heterogeneities at the crust-mantle interface.

4.7. Summary

The results presented here rely on the accuracy of the GRAIL models crustal thickness estimates, and the cratérisation equations. The results tend to show that there is an evolution of the composition of pyroxene with depth (from HCP to LCP), that may correspond to the transition between the crust and the mantle. Olivine and spinel detections are concentrated in a thin interval of the lower crust, however they do not seem to be linked with the emplacement of a specific layer like urKREEP material; but rather seem to have a plutonic origin. Plagioclase is detected widely in the crust, including in craters supposedly sampling lower crust to mantle material. However, other minerals like HCP, spinel, olivine, or pyroxene-dominated mixture spectra are also detected in most of the surveyed central peaks where plagioclase is detected. If a global anorthositic layer exists, as suggested by Donaldson Hanna et al. (2014), Ohtake et al. (2009), and Yamamoto et al. (2012), it may be mixed by subsequent impact events. According to impact simulations of Melosh et al. (2017), the lower crust to mantle is LCP-rich, also supported by the observations of LCP-enrichment with depth from Tompkins and Pieters (1999). The transition between HCP and LCP in our data occurs close to the model crust-mantle interface, and could correspond to the transition from crust to mantle. Moreover, plagioclase was not detected in craters where LCP occurrences are found. The transition from crust to mantle appears to be gradual, with plagioclase and pyroxene-dominated mixture spectra being observed throughout the investigated crustal and putative mantle column. The mineralogical observations reported in this study fit the GRAIL crustal thickness model 1 better than the model 3, although the small number of observations reported here does not allow strong conclusions to be drawn.

5. Conclusions

Spectroscopic data of a selection of 36 craters central peaks and peak rings distributed on the lunar surface, coupled with their P_{cmi} value, show that plagioclase is widely present throughout the crust, except in central peaks where LCP is detected. An evolution of pyroxene composition with depth that may correspond to the transition between the crust and the mantle is observed. According to the mineralogical detections reported here, a crust-mantle interface could be placed at P_{cmi} values between Humboldt and Maginus craters −1.2 km with GRAIL crustal thickness model 1, and +7.5 km with GRAIL crustal thickness model 3 for Humboldt crater; −2.0 km with GRAIL crustal thickness model 1, and +6.4 km with GRAIL crustal thickness model 3 for Maginus crater. Lateral heterogeneities seem to exist at the depth of the crust-mantle interface, as the HCP

detections and some pyroxene-dominated mixture spectra are situated close to maria and cryptomaria locations. The GRAIL crustal thickness model 1 fits these mineralogical detections better than model 3. This study illustrates how mineralogical detections in crater central peaks can be used to provide independent constraints on interior models.

Acknowledgments
We appreciated receiving positive and insightful reviews from Vivian Sun and an anonymous reviewer. We also thank the editors for their time. Jean-François Blanchette-Guertin provided useful inputs for the P_{cmi} value calculation. We thank Mark Wieczorek, Kerri Donaldson-Hanna, Makiko Ohtake, and Satoru Yamamoto for kindly sharing their data. This work was supported by a Netherlands Organization for Scientific Research (NWO) Vici grant and a User Support Space Research grant from the Netherlands Space Office (NSO) to W.v.W. J.F. is funded by APR-CNES Luna. C.Q.N. is supported by European Research Council through the FP7/2007-2013/ERC grant agreement 280168. M^3 and LRO data can be accessed in the PDS Geoscience Node, Lunar Orbital Data Explorer (http://ode.rsl.wustl.edu/). The global mosaic of the LRO WAC is available at https://astrogeology.usgs.gov/search/map/Moon/LRO/LROC_WAC/Lunar_LRO_LROC-WAC_Mosaic_global_100m_June2013. LRO LOLA/SELENE Terrain Camera merged stereo-derived digital elevation model can be found at https://astrogeology.usgs.gov/search/map/Moon/LRO/LOLA/Lunar_LRO_LrocKaguya_DEMmerge_60N60S_512ppd. The Lunar Impact Crater Database can be found at https://www.lpi.usra.edu/lunar/surface/Lunar_Impact_Crater_Database_v08Sep2015.xls The global maria shapefiles can be found in the LRO archive (http://lroc.sese.asu.edu/data/LRO-L-LROC-5-RDR-V1.0/LROLRC_2001/EXTRAS/SHAPEFILE/LROC_GLOBAL_MARE/). The cryptomaria shapefile can be found in the LPI concept 3 archive (https://www.lpi.usra.edu/exploration/CLSE-landing-site-study/). Laboratory spectra can be found in the RELAB spectral database archive (http://www.planetary.brown.edu/relab/).

References

Adams, J. B. (1974). Visible and near-infrared diffuse reflectance spectra of pyroxenes as applied to remote sensing of solid objects in the solar system. *Journal of Geophysical Research*, *79*(32), 4829. https://doi.org/10.1029/JB079i032p04829

Adams, J. B., & Goullaud, L. H. (1978). *Plagioclase feldspars: Visible and near infrared diffuse reflectance spectra as applied to remote sensing*. Proceedings of the Lunar and Planetary Science Conference (pp. 1205–1207).

Adams, J. B., Hörz, F., & Gibbons, R. V. (1979). *Effects of shock-loading on the reflectance spectra of plagioclase, pyroxene, and glass*. Proceedings of the 10th Lunar and Planetary Science Conference (pp. 5–7) Houston, TX.

Baker, D. M. H., & Head, J. W. (2015). Constraints on the depths of origin of peak rings on the Moon from Moon Mineralogy Mapper data. *Icarus*, *258*, 164–180. https://doi.org/10.1016/j.icarus.2015.06.013

Baker, D. M. H., Head, J. W., Fassett, C. I., Kadish, S. J., Smith, D. E., Zuber, M. T., & Neumann, G. A. (2011). The transition from complex crater to peak-ring basin on the Moon: New observations from the Lunar Orbiter Laser Altimeter (LOLA) instrument. *Icarus*, *214*(2), 377–393. https://doi.org/10.1016/j.icarus.2011.05.030

Besse, S., Sunshine, J., Staid, M., Boardman, J., Pieters, C., Guasqui, P., et al. (2013). A visible and near-infrared photometric correction for Moon Mineralogy Mapper (M^3). *Icarus*, *222*, 229–242. https://doi.org/10.1016/j.icarus.2012.10.036

Boardman, J. W., Pieters, C. M., Green, R. O., Lundeen, S. R., Varanasi, P., Nettles, J., et al. (2011). Measuring moonlight: An overview of the spatial properties, lunar coverage, selenolocation, and related Level 1B products of the Moon Mineralogy Mapper. *Journal of Geophysical Research*, *116*, 1–15. https://doi.org/10.1029/2010JE003730

Bruckenthal, E. A., & Pieters, C. M. (1984). *Spectral effects of natural shock on plagioclase felsdpar*. Proceedings of the 15th Lunar and Planetary Science Conference (pp. 96–97), Houston, TX.

Burns, R. G. (1970). Crystal field spectra and evidence of cation ordering in olivine minerals. *American Mineralogist*, *55*, 1608.

Burns, R. G. (1993). *Mineralogical applications of crystal field theory* (2nd ed.). Cambridge: Cambridge University Press. https://doi.org/10.1017/CBO9780511524899

Cahill, J. T. S., Lucey, P. G., & Wieczorek, M. A. (2009). Compositional variations of the lunar crust: Results from radiative transfer modeling of central peak spectra. *Journal of Geophysical Research*, *114*, 1–17. https://doi.org/10.1029/2008JE003282

Charlier, B., Grove, T. L., Namur, O., & Holtz, F. (2018). Crystallization of the lunar magma ocean and the primordial mantle-crust differentiation of the Moon. *Geochimica et Cosmochimica Acta*, *234*, 50–69. https://doi.org/10.1016/j.gca.2018.05.006

Cheek, L. C., Donaldson Hanna, K. L., Pieters, C. M., Head, J. W., & Whitten, J. L. (2013). The distribution and purity of anorthosite across the Orientale basin: New perspectives from Moon Mineralogy Mapper data. *Journal of Geophysical Research: Planets*, *118*, 1805–1820. https://doi.org/10.1002/jgre.20126

Cheek, L. C., & Pieters, C. M. (2014). Reflectance spectroscopy of plagioclase-dominated mineral mixtures: Implications for characterizing lunar anorthosites remotely. *American Mineralogist*, *99*(10), 1871–1892. https://doi.org/10.2138/am-2014-4785

Cintala, M. J., & Grieve, R. A. F. (1998). Scaling impact melting and crater dimensions: Implications for the lunar cratering record. *Meteoritics & Planetary Science*, *33*(4), 889–912. https://doi.org/10.1111/j.1945-5100.1998.tb01695.x

Clark, R. N., Pieters, C. M., Green, R. O., Boardman, J. W., & Petro, N. E. (2011). Thermal removal from near-infrared imaging spectroscopy data of the Moon. https://doi.org/10.1029/2010JE003751

Cloutis, E. A., Sunshine, J. M., & Morris, R. V. (2004). Spectral reflectance-compositional properties of spinels and chromites: Implications for planetary remote sensing and geothermometry. *Meteoritics \ & Planetary Science*, *39*(4), 545–565. https://doi.org/10.1111/j.1945-5100.2004.tb00918.x

Crown, D. A., & Pieters, C. M. (1987). Spectral properties of plagioclase and pyroxene mixtures and the interpretation of lunar soil spectra. *Icarus*, *72*(3), 492–506. https://doi.org/10.1016/0019-1035(87)90047-9

Donaldson Hanna, K. L., Cheek, L. C., Pieters, C. M., Mustard, J. F., Greenhagen, B. T., Thomas, I. R., & Bowles, N. E. (2014). Global assessment of pure crystalline plagioclase across the Moon and implications for the evolution of the primary crust. *Journal of Geophysical Research: Planets*, *119*, 1516–1545. https://doi.org/10.1002/2013JE004476

Dygert, N., Lin, J.-F., Marshall, E. W., Kono, Y., & Gardner, J. E. (2017). A low viscosity lunar magma ocean forms a stratified anorthitic flotation crust with mafic poor and rich units. *Geophysical Research Letters*, 1–10. https://doi.org/10.1002/2017GL075703

Elardo, S. M., Draper, D. S., & Shearer, C. K. (2011). Lunar magma ocean crystallization revisited: Bulk composition, early cumulate mineralogy, and the source regions of the highlands Mg-suite. *Geochimica et Cosmochimica Acta*, *75*(11), 3024–3045. https://doi.org/10.1016/j.gca.2011.02.033

Elkins-Tanton, L. T., Burgess, S., & Yin, Q. Z. (2011). The lunar magma ocean: Reconciling the solidification process with lunar petrology and geochronology. *Earth and Planetary Science Letters*, *304*(3-4), 326–336. https://doi.org/10.1016/j.epsl.2011.02.004

Flahaut, J., Blanchette-Guertin, J.-F., Jilly, C., Sharma, P., Souchon, A., Van Westrenen, W., & Kring, D. A. (2012). Identification and characterization of science-rich landing sites for lunar lander missions using integrated remote sensing observations. *Advances in Space Research*, *50*(12), 1647–1665. https://doi.org/10.1016/j.asr.2012.05.020

Green, R. O., Pieters, C., Mouroulis, P., Eastwood, M., Boardman, J., Glavich, T., et al. (2011). The Moon Mineralogy Mapper (M_3) imaging spectrometer for lunar science: Instrument description, calibration, on-orbit measurements, science data calibration and on-orbit validation. *Journal of Geophysical Research*, *116*, 1–31. https://doi.org/10.1029/2011JE003797

Gross, J., Treiman, A. H., & Le, L. (2011). Unique spinel-rich lithology in lunar meteorite ALHA81005: Origin and possible connection to M_3 observations of the farside highlands. *Lunar and Planetary Science Conference*, *42*, 2–3.

Hawke, B. R., Peterson, C. A., Blewett, D. T., Bussey, D. B. J., Lucey, P. G., Taylor, G. J., & Spudis, P. D. (2003). Distribution and modes of occurrence of lunar anorthosite. *Journal of Geophysical Research*, *108*(E6), 1–16. https://doi.org/10.1029/2002JE001890

Head, J. W., Murchie, S., Mustard, J. F., Pieters, C. M., Neukum, G., McEwen, A., et al. (1993). Lunar impact basins: New data for the western limb and far side (Orientale and South Pole-Aitken Basins) from the first Galileo flyby. *Journal of Geophysical Research*, *98*(E9), 17149–17182.

Head, J. W., & Wilson, L. (1992). Lunar mare volcanism: Stratigraphy, eruption conditions, and the evolution of secondary crusts. *Geochimica et Cosmochimica Acta*, *56*(6), 2155–2175. https://doi.org/10.1016/0016-7037(92)90183-J

Horgan, B. H. N., Cloutis, E. A., Mann, P., & Bell, J. F. (2014). Near-infrared spectra of ferrous mineral mixtures and methods for their identification in planetary surface spectra. *Icarus*, *234*, 132–154. https://doi.org/10.1016/j.icarus.2014.02.031

Howard, K. A., Wilhelms, D. E., & Scott, D. H. (1974). Lunar basin formation and highland stratigraphy. *Reviews of Geophysics*, *12*(3), 309–327. https://doi.org/10.1029/RG012i003p00309

Hurwitz, D. M., & Kring, D. A. (2014). Differentiation of the South Pole-Aitken basin impact melt sheet: Implications for lunar exploration. *Journal of Geophysical Research: Planets*, *119*, 1110–1133. https://doi.org/10.1002/2014JE004657

Isaacson, P. J., Pieters, C. M., Besse, S., Clark, R. N., Head, J. W., Klima, R. L., et al. (2011). Remote compositional analysis of lunar olivine-rich lithologies with Moon Mineralogy Mapper (M_3) spectra. *Journal of Geophysical Research*, *116*, 1–17. https://doi.org/10.1029/2010JE003731

Jaumann, R., Hiesinger, H., Anand, M., Crawford, I. A., Wagner, R., Sohl, F., et al. (2012). Geology, geochemistry, and geophysics of the Moon: Status of current understanding. *Planetary and Space Science*, *74*(1), 15–41. https://doi.org/10.1016/j.pss.2012.08.019

Jolliff, B. L., Gillis, J. J., Haskin, L. A., Korotev, R. L., & Wieczorek, M. A. (2000). Major lunar crustal terranes: Surface expressions and crust-mantle origins. *Journal of Geophysical Research*, *105*(E2), 4197. https://doi.org/10.1029/1999JE001103

Jozwiak, L. M., Head, J. W., Zuber, M. T., Smith, D. E., & Neumann, G. A. (2012). Lunar floor-fractured craters: Classification, distribution, origin and implications for magmatism and shallow crustal structure. *Journal of Geophysical Research*, *117*, 1–23. https://doi.org/10.1029/2012JE004134

Kaula, W. M. (1979). Thermal evolution of Earth and Moon growing by planetesimal impacts. *Journal of Geophysical Research*, *84*(2), 999–1008. https://doi.org/10.1029/JB084iB03p00999

Klima, R. L., Pieters, C. M., & Dyar, M. D. (2007). Spectroscopy of synthetic Mg-Fe pyroxenes I: Spin-allowed and spin-forbidden crystal field bands in the visible and near-infrared. *Meteoritics \ & Planetary Science*, *42*(2), 235–253. https://doi.org/10.1111/j.1945-5100.2007.tb00230.x

Kring, D. A., Durda, D. D., Sullivan, K. O., Barnes, J., Blair, D. M., Runyon, K. D., et al. (2012). A global lunar landing site study to provide the scientific context for exploration of the Moon. 695.

Lemelin, M., Lucey, P. G., Song, E., & Taylor, G. J. (2015). Lunar central peak mineralogy and iron content using the Kaguya Multiband Imager: Reassessment of the compositional structure of the lunar crust. *Journal of Geophysical Research: Planets*, *120*, 869–887. https://doi.org/10.1002/2014JE004778

Lin, Y., Tronche, E. J., Steenstra, E. S., & van Westrenen, W. (2017a). Experimental constraints on the solidification of a nominally dry lunar magma ocean. *Earth and Planetary Science Letters*, *471*, 104–116. https://doi.org/10.1016/j.epsl.2017.04.045

Lin, Y., Tronche, E. J., Steenstra, E. S., & van Westrenen, W. (2017b). Evidence for an early wet Moon from experimental crystallization of the lunar magma ocean. *Nature Geoscience*, *10*(1), 1–6. https://doi.org/10.1038/ngeo2845

Losiak, A., Wilhelms, D. E., Byrne, C. J., Thaisen, K., Weider, S. Z., Kohout, T., et al. (2009). *A new lunar impact crater database*. Proceedings of the 40th Lunar and Planetary Science Conference Houston, TX.

Lucey, P. G. (2002). Radiative transfer model constraints on the shock state of remotely sensed lunar anorthosites. *Geophysical Research Letters*, *29*(10), 1486. https://doi.org/10.1029/2001GL014655

Martinot, M., Besse, S., Flahaut, J., Quantin-Nataf, C., Lozac'h, L., & van Westrenen, W. (2018). Mineralogical diversity and geology of Humboldt crater derived using Moon Mineralogy Mapper data. *Journal of Geophysical Research: Planets*, *123*, 612–629. https://doi.org/10.1002/2017JE005435

Melosh, H. J., Kendall, J., Horgan, B., Johnson, B. C., Bowling, T., Lucey, P. G., & Taylor, G. J. (2017). South Pole-Aitken basin ejecta reveal the Moon's upper mantle. *Geology*, *45*(12), 1063–1066. https://doi.org/10.1130/G39375.1

Miljković, K., Lemelin, M., & Lucey, P. G. (2017). Depth of origin of the peak (inner) ring in lunar impact basins. *Geophysical Research Letters*, *44*, 10,140–10,146. https://doi.org/10.1002/2017GL075207

Morrison, D. A. (1998). *Did a thick South Pole-Aitken basin melt sheet differentiate to form cumulates?* Proceedings to the 29th Lunar and Planetary Science Conference (pp. 2–3), Houston, TX.

Mustard, J. F., & Pieters, C. M. (1987). Quantitative abundance estimates from bidirectional reflectance measurements. *Journal of Geophysical Research*, *92*(B4), E617–E626. https://doi.org/10.1029/JB092iB04p0E617

Nakamura, R., Matsunaga, T., Ogawa, Y., Yamamoto, S., Hiroi, T., Saiki, K., et al. (2009). Ultramafic impact melt sheet beneath the South Pole-Aitken basin on the Moon. *Geophysical Research Letters*, *36*, L22202. https://doi.org/10.1029/2009GL040765

Ohtake, M., Matsunaga, T., Haruyama, J., Yokota, Y., Morota, T., Honda, C., et al. (2009). The global distribution of pure anorthosite on the Moon. *Nature*, *461*(7261), 236–240. https://doi.org/10.1038/nature08317

Pieters, C. M., Besse, S., Boardman, J., Buratti, B., Cheek, L., Clark, R. N., et al. (2011). Mg-spinel lithology: A new rock type on the lunar farside. *Journal of Geophysical Research*, *116* E00G08. https://doi.org/10.1029/2010JE003727

Pieters, C. M., Boardman, J., Buratti, B., Chatterjee, A., Clark, R., Glavich, T., et al. (2009). The Moon Mineralogy Mapper (M^3) on Chandrayaan-1. *Current Science*, *96*(4), 1–6.

Pieters, C. M., Head, J. W., Sunshine, J. M., Fischer, E. M., Murchie, S. L., Belton, M., et al. (1993). Crustal diversity of the Moon: Compositional analyses of Galileo solid state imaging data. *Journal of Geophysical Research*, *98*, 17,127–17,148.

Pieters, C. M., Kerri Donaldson, H., Cheek, L., Dhingra, D., Prissel, T., Jackson, C., et al. (2014). The distribution of Mg-spinel across the Moon and constraints on crustal origin. *American Mineralogist*, *99*(10), 1893–1910. https://doi.org/10.2138/am-2014-4776

Rapp, J. F., & Draper, D. S. (2018). Fractional crystallization of the lunar magma ocean : Updating the dominant paradigm. *Meteoritics \ & Planetary Science*, *24*, 1–24. https://doi.org/10.1111/maps.13086

Shearer, C. K., Hess, P. C., Wieczorek, M. A., Pritchard, M. E., Parmentier, E. M., Borg, L. E., et al. (2006). Thermal and magmatic evolution of the Moon. *Reviews in Mineralogy and Geochemistry*, *60*(1610), 365–518. https://doi.org/10.2138/rmg.2006.60.4

Snyder, G. A., Taylor, L. A., & Neal, C. R. (1992). A chemical model for generalting the sources of mare basalts: Combined equilibrium and fractional crystallization of th elunar magmasphere. *Geochimica et Cosmochimica Acta*, *56*, 3809–3823.

Song, E., Bandfield, J. L., Lucey, P. G., Greenhagen, B. T., & Paige, D. A. (2013). Bulk mineralogy of lunar crater central peaks via thermal infrared spectra from the Diviner Lunar Radiometer: A study of the Moon's crustal composition at depth. *Journal of Geophysical Research: Planets*, *118*, 689–707. https://doi.org/10.1002/jgre.20065

Spudis, P. D., Gillis, J. J., & Reisse, R. A. (1994). Ancient multiring basins on the moon revealed by clementine laser altimetry. *Science (New York, N.Y.)*, *266*(5192), 1848–1851. https://doi.org/10.1126/science.266.5192.1848

Spudis, P. D., Hawke, B. R., & Lucey, P. (1984). Composition of orientale basin deposits and implications for the lunar basin-forming process. *Journal of Geophysical Research*, *89*(S01), C197–C210. https://doi.org/10.1029/JB089iS01p0C197

Sunshine, J. M., & Pieters, C. M. (1998). Determing the composition of olivine from reflectance spectroscopy. *Journal of Geophysical Research*, *103*, 675–688.

Tompkins, S., & Pieters, C. M. (1999). Mineralogy of the lunar crust: Results from Clementine. *Meteoritics \ & Planetary Science*, *34*, 25–41.

Vaughan, W. M., Head, J. W., Wilson, L., & Hess, P. C. (2013). Geology and petrology of enormous volumes of impact melt on the Moon: A case study of the Orientale basin impact melt sea. *Icarus*, *223*(2), 749–765. https://doi.org/10.1016/j.icarus.2013.01.017

Warren, P. H. (1985). The magma ocean concept and lunar evolution. *Annual Review of Earth and Planetary Science*, *13*, 201–40. https://doi.org/10.1146/annurev.earth.13.1.201

Warren, P. H., & Wasson, J. T. (1979). The origin of KREEP. *Reviews of Geophysics and Space Physics*, *17*(1). https://doi.org/10.1029/RG017i001p00073

Whitten, J. L., & Head, J. W. (2015). Lunar cryptomaria: Physical characteristics, distribution, and implications for ancient volcanism. *Icarus*, *247*, 150–171. https://doi.org/10.1016/j.icarus.2014.09.031

Wieczorek, M. A., Neumann, G. A., Nimmo, F., Kiefer, W. S., Taylor, G. J., Melosh, H. J., et al. (2013). The crust of the Moon as seen by GRAIL. *Science (New York, N.Y.)*, *339*(6120), 671–5. https://doi.org/10.1126/science.1231530

Wieczorek, M. A., & Phillips, R. J. (2000). The "Procellarum KREEP Terrane": Implications for mare volcanism and lunar evolution. *Journal of Geophysical Research*, *105*(E8), 20417–20430.

Yamamoto, S., Nakamura, R., Matsunaga, T., Ogawa, Y., Ishihara, Y., Morota, T., et al. (2010). Possible mantle origin of olivine around lunar impact basins detected by SELENE. *Nature Geoscience*, *3*(8), 533–536. https://doi.org/10.1038/ngeo897

Yamamoto, S., Nakamura, R., Matsunaga, T., Ogawa, Y., Ishihara, Y., Morota, T., et al. (2012). Massive layer of pure anorthosite on the Moon. *Geophysical Research Letters*, *39*, L13201. https://doi.org/10.1029/2012GL052098

Yamamoto, S., Nakamura, R., Matsunaga, T., Ogawa, Y., Ishihara, Y., Morota, T., et al. (2015). Featureless spectra on the Moon as evidence of residual lunar primordial crust. *Journal of Geophysical Research: Planets*, *120*, 2190–2205. https://doi.org/10.1002/2015JE004935